Nanoscale Advances

ROYAL SOCIETY OF CHEMISTRY

PAPER

View Article Online
View Journal | View Issue

Cite this: *Nanoscale Adv.*, 2023, **5**, 3905

A robust MRI contrast agent for specific display of the interstitial stream†

Xiaohan Zhou, ‡[ac] Junwei Cheng,‡[b] Fangfei He,[ab] Zhuo Ao,[ac] Peisen Zhang,[b] Jing Wang,[d] Qing Li,[e] Weinan Tang,[af] Yiyan Zhou,[g] Yan Liang,[ac] Yi Hou, *[b] Wentao Liu *[ac] and Dong Han *[ac]

Experimental and clinical studies have reported phenomena of long-range fluid flow in interstitial space. However, its behaviours and functions are yet to be addressed. The imaging of the interstitial stream *in vivo* can clarify its transportation route and allow further understanding of physiological mechanisms and clinical relevance. Here to illustrate the route of the interstitial stream leading to the kidney, we design and synthesize a magnetic resonance imaging (MRI) contrast agent PAA-*g*-(DTPA-gadolinium). This MRI agent has a high longitudinal relaxivity for higher MRI contrast and large size to avoid leakage across the interstitial space. Using dynamic contrast enhanced MRI, histochemical staining, and trace element analysis of gadolinium, we track the nano-scale PAA-*g*-(DTPA-gadolinium) transported in the interstitial stream. The agent can be applied for a wide range of imaging and analysis of tissues and organs, thereby enabling advances in the fields of physiology, pathology, and pharmacology.

Received 24th February 2023
Accepted 26th May 2023

DOI: 10.1039/d3na00118k

rsc.li/nanoscale-advances

1. Introduction

The interstitial stream in tissues and among organs is a major component of fluid flow in hierarchical porous media in humans. Tissue channels rich in water molecules form connective paths in the interstitium,[1] which is a randomly distributed porous network containing loose connective tissue (LCT) as a major component.[2,3] However, the functions and applications of the tissue channel remain largely undefined in the literature. Although research on interstitial space has revealed many structural and distributional aspects, its technical foundations remain vague.

Two-photon microscopy revealed that the glymphatic system[4] functions as a metabolite clearance pathway through the brain parenchyma. This result provided considerable insight into the effect of interstitial behaviour on the mechanism and function of transportation.[5] A long-range transport in LCT along veins was found, and detailed research on artificial fibre networks was performed to simulate the transportation speed described by Fick's law.[6,7] Previous *in vitro* studies have confirmed LCT long-range transmission by using atomic force microscopy (AFM) cantilever knocking at the end of the adventitia of the blood vessel and have characterised the super lubrication of LCT.[7–9] These studies have focused on the biodistribution and transportation of nanoparticles and liquid metals, and have confirmed directional transport, which differed from that of blood transport over long distances.[10,11]

The results of the studies have revealed that the body surface, limbs, and viscera can be efficiently connected by the interstitial stream.[12] However, the connectivity and paths remain unclear. The complexity of the hierarchical interstitium networks encapsulating cells, tissues, and organs increases the difficulty in predicting the interstitial stream-flow behaviour. Interstitium characterisation, particularly in terms of its structure and function, has attracted considerable research attention.[13]

Ex vivo experiments were performed on amputated lower limbs and donated bodies,[14,15] and chest compressors were applied as an additional external force. The results of the study revealed that passive transport occurs along the interstitial stream as pseudo-phenomena. Prior knowledge reveals that the chemical constituents inside the interstitial stream contain a collagen interfiber network and matrix gels,[6,7] and the formed elastic filaments enable the exhibition of distinct rheological properties.[2]

[a]*CAS Center for Excellence in Nanoscience, National Center for Nanoscience and Technology, Beijing, 100190, China. E-mail: liuwentao@nanoctr.cn; dhan@nanoctr.cn*

[b]*College of Life Science and Technology, Beijing University of Chemical Technology, Beijing, 100029, China. E-mail: houyi@iccas.ac.cn*

[c]*University of Chinese Academy of Sciences, Beijing 100139, China*

[d]*Center for Medical Device Evaluation, NMPA, Beijing 100081, China*

[e]*Department of Nutrition, Southwest Hospital, Third Military Medical University (Army Medical University), Chongqing, 400038, China*

[f]*Beijing Wandong Medical Technology Co., Beijing 100015, China*

[g]*College of Biological Sciences, University of California at Davis, Sacramento, CA, 95817, USA*

† Electronic supplementary information (ESI) available. See DOI: https://doi.org/10.1039/d3na00118k

‡ These authors contributed to the work equally.

The certain amount of water in the interstitial stream necessitates an efficient method for detecting the mass transportation of the contrast agent. Compared with computed tomography or positron emission tomography, magnetic resonance imaging (MRI) is a non-invasive monitoring technique and exhibits excellent soft-tissue imaging performance.[16] The application of protons macroscopic polarisation[17] without radiation exposure presents an approach for long-term *in situ* intravital scanning. At a clinical magnetic field strength (3 Tesla and below), MRI results revealed a low spatial resolution and diminished signal-to-noise ratio (SNR) efficiency at a high field strength.[18] However, a prolonged longitudinal time at high field strengths and high resolutions is required to characterise biological tissues to obtain a high SNR.

Therefore, medical contrast agents are used to reduce the longitudinal relaxation time[19] and decrease the scan time required for obtaining the MRI sequence. In this study, a macromolecular MRI contrast agent was used *via* interstitial space injection (ISI)[10,20] to accomplish *in vivo* study and enhance the contrast of the interstitial stream *in situ* during scanning. The injection gap positions at the tarsal tunnel consist of connective tissue which is connected to the interstitial stream. We used the macromolecule agent chelated with a long-chain Gd^{3+} to exhibit an interstitial stream and test its longitudinal relaxivity and permeability across vessels. Besides, in our study, dynamic contrast enhanced (DCE) MRI[21] was performed to illustrate the feasibility of the polyacrylic acid-*g*-(DTPA-gadolinium) (PAA-Gd) agent on interstitial stream imaging, and a histochemical study was conducted to validate this approach from the microscopic perspective for further insights.

2. Results

2.1. Synthesis and characterisation of PAA-Gd

The synthesis result of the zwitterionic MCP (metal-chelating polymers) contrast agent, namely, PAA-Gd is depicted on the right-hand side of Fig. 1a as an elongated chain. As shown in Fig. 1a, DTPAs were covalently linked to the side chains of PAA through diethylenetriamine (DET) linkers *via* the amidation reaction, which was catalysed through 4-(4,6-dimethoxy-1,3,5-triazin-2-yl)-4-methyl-morpholinium chloride (DMTMM). The PAA-Gd contrast agent was obtained through the coordination of residual carboxyl groups of DTPA and Gd^{3+}. The hydrodynamic size of the PAA-Gd macromolecule is approximately 6–7 nm (Fig. 1c).

The ^{1}H NMR spectra of PAANa (sodium polyacrylate), PAA-DET, and PAA-DTPA, in each synthesis step of the zwitterionic MCP contrast agent PAA-Gd, are displayed in Fig. 1b. The proton signals of methylene and methylidyne on the backbone of PAANa (a and b) appeared at 1.4 and 2.0 ppm, respectively. After conjugation with DET and DTPA, the proton signals of the methylene of DET appeared at c, d, e, and f, and the proton signals of the methylene of DTPA appeared at g, h, i, and j in the range of 2.7–4.0 ppm. The proton signals of the backbone moved slightly into a higher magnetic field, indicating that DET and DTPA were successfully combined with the main chain of PAANa.

Each side of the DTPA has four residual carboxyl groups to coordinate with Gd^{3+}; hence, there is an excess negative charge. Moreover, the acidity coefficient (pK_a) of the secondary amine[22] (–NH–) in DET is higher than 10; thus, the secondary amine presents a positive charge under neutral or physiological conditions due to protonation. The adjacent positive and negative charges constitute the zwitterionic side groups of PAA-Gd. Accordingly, after connecting to DET and DTPA and coordinating with Gd^{3+}, the electrophoretic mobility was $(-2.855 \pm 0.298) \times 10^8$ m^2 V^{-1} s^{-1}, $(0.343 \pm 0.071) \times 10^8$ m^2 V^{-1} s^{-1}, $(-3.046 \pm 0.224) \times 10^8$ m^2 V^{-1} s^{-1}, and $(-1.347 \pm 0.175) \times 10^8$ m^2 V^{-1} s^{-1}, respectively (Fig. 1d). This variation of the electrophoretic mobility hints at the successful synthesis of the zwitterionic PAA-Gd molecule after the multi-step reaction described above.

2.2. Cytotoxicity test on the agent

The macromolecule compound PAA-Gd exhibits low cytotoxicity towards mammalian cells according to a cytotoxicity study conducted through the CCK-8 test on human umbilical vein endothelial cells (HUVECs). Compared with Gd-DTPA, PAA-Gd exhibited higher viability, particularly at higher levels of the Gd^{3+} concentration (Fig. 1f).

2.3. MR phantom study of the PAA-Gd agent

A series of T_1 values of PAA-Gd at various doses given in the water phantom were measured with the T_1 mapping sequence. The signal intensity of the phantom with different levels of Gd^{3+} is displayed in Fig. 1e (top left panel). As R_1 data were calculated from the T_1 value according to eqn (1) in the ESI,† the relaxation rate of the aqueous solution after enhancement agent shortening is the inverse of the T_1 value. By curve fitting (Fig. 1e), the regression function of the relaxation rate according to the Gd^{3+} concentration (C) is mathematically expressed as follows: $R_1(C) = 13.94C + 0.75$ ($R^2 = 0.999$). $R_{1\mathrm{obs}}(C) = r_{1\mathrm{p}}[C] + r_{1\mathrm{d}}$ where $r_{1\mathrm{p}}$ and $r_{1\mathrm{d}}$ are the relaxivity of the Gd(III)-complex and the diamagnetic relaxation rate, respectively. The longitudinal relaxivity of PAA-Gd was obtained from the slope of the curve as 13.94 mM^{-1} s^{-1} under 1.5 Tesla and 5.88 mM^{-1} s^{-1} under 7 Tesla.

The relaxivity value of Gd-DTPA (Magnevist) was measured as 3.05 mM^{-1} s^{-1} under the same experimental conditions at 21 °C under a magnetic field of 1.5 Tesla.[23]

2.4. *In vivo* MR imaging

All animal study procedures were performed under the supervision of the Ethics Committee at the National Center for Nanoscience and Technology and in compliance with the handling guidelines and protocols for use, maintenance, and care of laboratory animals; the approved ethics document ID was NCNST21-2011-0612.

The DCE results revealed the change in the signal intensity of ROIs with the time series. Immediately after PAA-Gd injection through the ISI at the tarsal tunnel, the MRI signal intensity became high in response to the intense increase in the local Gd^{3+} concentration, which resulted in decreased local T_1 values in eqn (1). The first two adjacent time points were presented

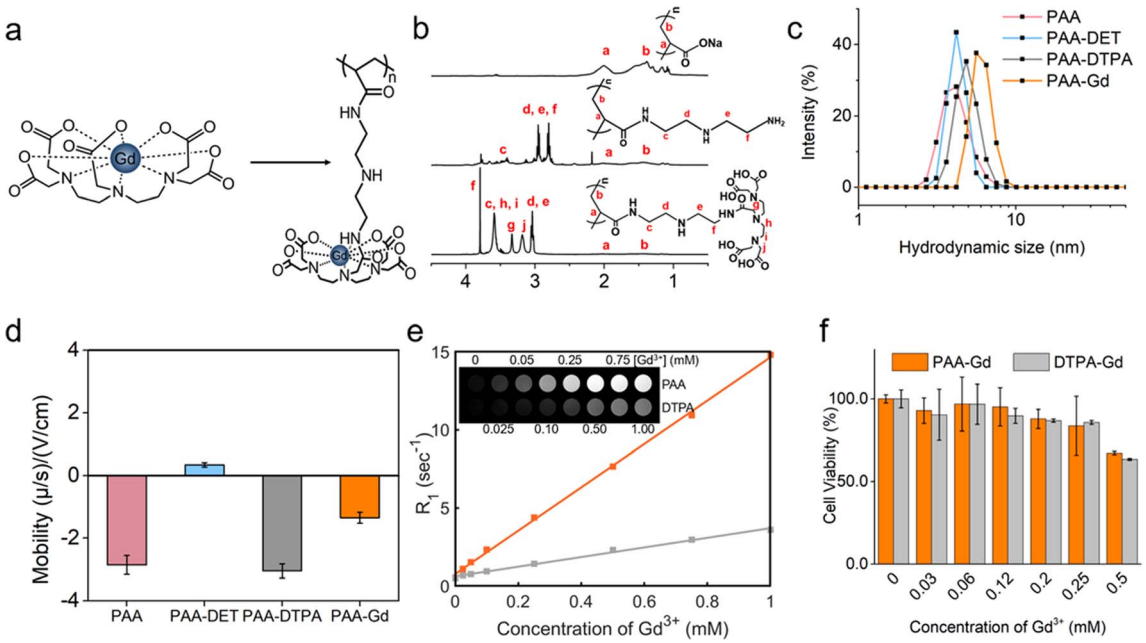

Fig. 1 Phantom characterisation and MR test. (a) Chemical structures of the DTPA-Gd agent compared with the PAA-Gd macromolecule linked in a long chain (see also Fig. S4†). (b) ^{1}H NMR spectrum of PAA, PAA-DET, and PAA-DTPA, in the top, middle, and bottom panels respectively. (c) and (d) The hydrodynamic size and electrophoretic mobility of PAA, PAA-DET, PAA-DTPA, and PAA-Gd in a hydrophilic solvent, respectively. (e) Linear regression fitting curve (solid line) of the calculated R_1 value (squares). Top panel: signal intensity map of T_1 weighted MR images (TE = 10 ms, TR = 200 ms, and flip angle = 90°) of an aqueous solution of PAA-Gd in 2.0 mL Eppendorf tubes according to different Gd^{3+} concentrations. (f) Viabilities of HUVE cells treated with PAA-Gd and Gd-DTPA with various dosages.

among 150 repetitions along with DCE time courses (Fig. 2b), which are also illustrated in ESI Movie 3.†

Because of the compactness and continuity of fasciae along the ankle and leg, the macromolecule compound PAA-Gd (MW: 5100 Da and hydrodynamic diameter: 6–7 nm), with its dynamic light scattering result displayed in Fig. 1c, exists on one side of the interstitial stream[10] (Fig. 3g and h). This accumulation of PAA-Gd at the injection point led to high local signal intensity. As displayed in Fig. 2b, the inner pressure motivated the flow of the macromolecule agent along the pathway, which required approximately one or two scan cycles (7.68 s). The DCE result shows that the pathway took 222.72 s to reach the peak signal enhancement in the interstitial stream, and the hyperintensity decreased slowly with time, while the initial enhancement occurs at 38.6 s post-injection. For the pathway of PAA-Gd (Fig. 2a), the nano-scale PAA-Gd agent was transported along the fibre bundles (blue coloured structures in Fig. 2a) because of its large size (Fig. 1a and c) and high longitudinal relaxivity (Fig. 1e).

DCE imaging was performed for 20 min on the kidney plane (Fig. 4a, ESI Movies 2 and 3†). The PAA-Gd delineated the renal hilus and cortex starting 5 min post-injection and lasted for more than 15 min, and the signal intensity strongly increased at the site of the hilus where the adventitia of the blood vessels merged into the tissue (Fig. 4c). This is further illustrated with a scheme in Fig. 4b. The mechanism of PAA-Gd transport in the interstitial stream is illustrated on the right side of Fig. 2a.

2.5. *Ex vivo* histological staining results of ISI with PAA-Gd

Fig. 3g and h display the coronal view of the kidney on the renal hilus plane dyed with CPN III, which revealed the mass deposition of Gd^{3+} at the renal cortex and hilus. The red blood cells were dyed brown on the CPN III section, which indicated low leakage of PAA-Gd from the interstitial space. The histological study was consistent with the radiology results of the continuous research on the same mouse injected with PAA-Gd.

To discuss the behaviour and function of PAA-Gd through ISI at a microcosmic level, a histology study was performed with the same injection protocols, and its results were in accordance with the MRI results (Fig. 4a, c and d). The staining approach for rare-earth-containing probes upon CPN III was verified[24] based on the chromogenic reaction from violet to green. The mice were categorised into the ISI and intravenous injection (IVI) groups, and their kidneys were harvested 6 min post-injection when the rate of increase of signal intensity at the renal cortex and hilum reduced according to DCE displays. The histopathological information of the kidneys was obtained from Masson and hematoxylin–eosin (H&E) staining, and the adjacent slice stained with CPN III revealed the PAA-Gd content. Fig. 3g displays the biodistribution of Gd^{3+} at the renal cortex and hilum for the ISI group. In the 20× section (Fig. 3h), the LCT at the renal hilum was dyed to deep green because of the high content level of local Gd^{3+}. Further semi-quantitative analysis was performed to compare the ISI and IVI groups (ESI Fig. 2†).

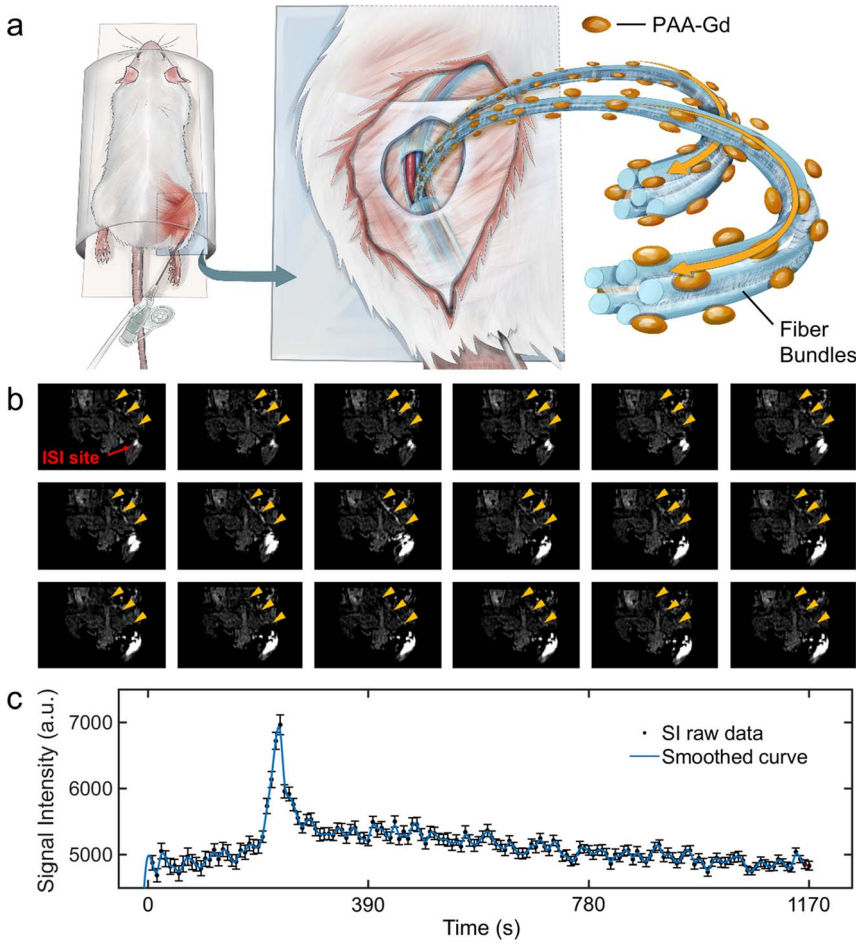

Fig. 2 Real-time imaging of PAA-Gd that revealed the pathway (interstitial stream transport) starting from the ISI site. (a) Schematic of PAA-Gd led by the interstitial stream. The scheme displays *in vivo* experiments performed on mice with PAA-Gd through ISI in the MRI scanner table. The needle was positioned at the tarsal tunnel in the leg of the mice with PAA-Gd (1 mM), and then the MR images were collected *in situ*. The macromolecule was restrained inside the interstitial space and transported along the narrow path formed by fasciae (displayed as the transparent membrane). The hydrogen-containing compounds (blue bundles) parallel the transportation direction of the PAA-Gd agent (orange). (b) The sequential frames of DCE images at the ISI site section slice. The interval is 7.68 s between each adjacent image. The signal of enhancement is observed and emphasised (with an orange arrow). (c) The signal intensity fluctuation along the time sequence in 19.5 min. (Data are represented as mean ± S.D.)

2.6. Comparison of ISI and IVI using PAA-Gd

The agent injected through the tail vein produced the first-pass effect in the vascular system (arteries are marked with blue arrows) and simultaneously converged on the renal pelvis (Fig. 5b). Inductively coupled plasma mass spectrometry (ICP-MS) was performed to quantitatively measure the absolute mass of the gadolinium element in tissues after the MRI study. The subcutaneous injection was applied as a negative control for the ISI group. Fig. 5c indicates that the gadolinium content in the tissues of the ISI group was uneven, and the content was higher in vein samples than in the IVI group. The removal of blood after enucleating the eyeballs was difficult, and hence all the values were divided by the outcome indices in the blood sample to achieve relative normalisation. The histological results substantiated more details about the distribution in the ISI and IVI groups. The content of gadolinium was low in blood for both ISI and IVI groups (Fig. 5d–g, red arrows) and high in LCTs six minutes after injection for the ISI group (Fig. 5f); a smooth muscle layer of the artery (blue arrows) was formed in the ISI group. The tunica interna of the artery is indicated in purple in Fig. 5f, which implied a low content of Gd^{3+}.

3. Discussion

In this work, imaging was conducted on the interstitial stream to determine the pathway from the subcutaneous tissue to the kidney. The high relaxivity and hydrodynamic size of the PAA-Gd agent promote its specificity for interstitial transportation. The signal enhancement in the MR image outlining the interstitial stream pathway is derived from the ISI position with the PAA-Gd agent, which terminates at the kidney. The radiological result, combined with the subsequent *ex vivo* histological and ICP-MS results, confirms the low content of gadolinium in blood. Furthermore, the long retention in the interstitial stream *via* ISI indicates the long-range fluid behaviour of nanoscale materials.

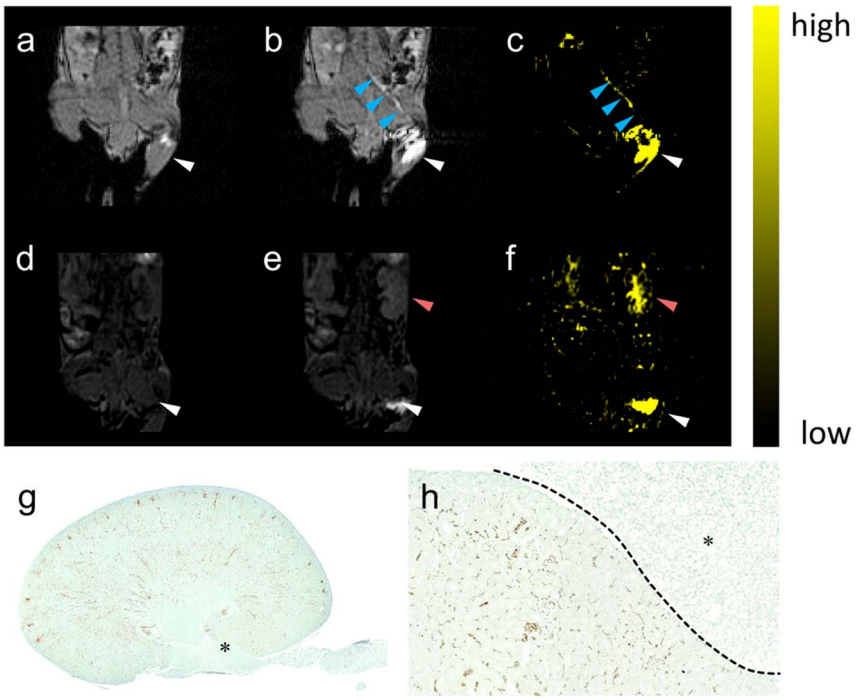

Fig. 3 The pathway lightened by PAA-Gd terminating at the kidney. (a) DCE images collected at (a) 0 and (b) 7.68 s post-injection on the coronal section of the injection plane according to the transparent blue plane displayed in Fig. 2b, and the image on the centric plane of the kidney (d) before and (e) 6 min after ISI (the increase in signal intensity at the renal cortex was marked with red arrow). Here, (c) and (f) show the subtraction of (c) to (b) and of (f) to (e) respectively. The injection site (white arrow) and transportation routine (blue arrow) were emphasised. DCE imaging is followed by histological staining with the kidney stained with CPN III (g) and the magnified view at 20 times (h) on the edge of the renal hilus after ISI injection of PAA-Gd.

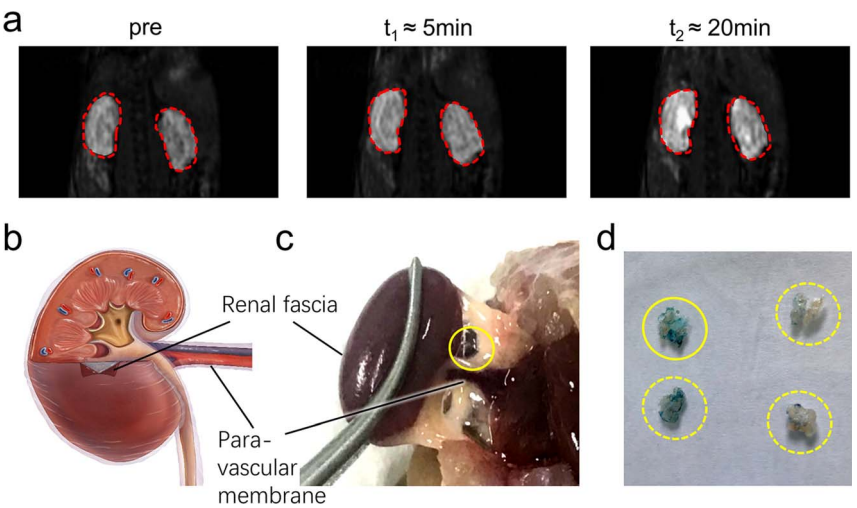

Fig. 4 MR images indicating that PAA-Gd was distributed at the renal cortex and the renal hilum. (a) MR images collected at t_0, t_1, and t_2 in the magnified view of the kidneys outlined with red solid lines. (b) Schematic of the renal anatomy structure. (c) Close-up view of the dissected kidney from the same animal in the MR image at the corresponding position. The moist membrane is emphasised with a yellow circle and corresponds to the transparent membrane coating the kidney in (b). (d) The LCT from the renal hilus and dyed with CPN III at the appropriate place in (c). Dashed lines indicate parallel experimental results from other mice under the same protocols.

3.1. Characteristics of the PAA-Gd agent

Due to the increase in τ_R (rotational correlation time) of PAA-Gd compared with Gd-DTPA,[25] the relaxivity of PAA-Gd is higher than that of Gd-DTPA,[26,27] which is a clinically implemented Gd^{3+}-based MRI contrast agent. Thus, the PAA-Gd agent can generate high signal intensity and contrast-to-noise ratio (CNR) with low concentration compared with Gd-DTPA.[23]

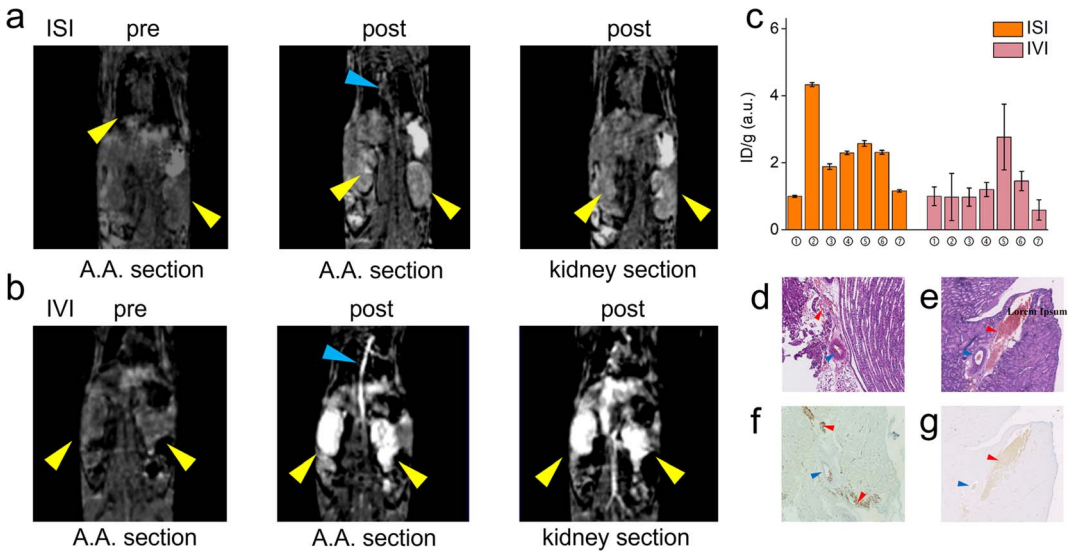

Fig. 5 Comparison of ISI group *versus* IVI group. (a) DCE images of the ISI group pre-injection *versus* post-injection at the centric plane of the right kidney, artery, and left kidney (from left to right); (b) that of the IVI group. (c) The relative gadolinium content in tissues collected from ISI, IVI, and ID (intradermal injection) groups. Samples from number one to seven are as follows: ① blood sample, ② ipsilateral femoral vein of injection, ③ heterolateral femoral vein of injection, ④ abdominal aorta of injection, ⑤ heterolateral renal vein of injection, ⑥ ipsilateral renal vein of injection, and ⑦ mesentery (data were represented as mean ± S.D. and asterisks indicate significant differences). (d) and (e) H&E staining sections of the renal parenchyma from ISI and IVI groups. (f) and (g) Histochemical staining sections of the adjacent slices to (d) and (e) dying with CPN III. Red blood cells (red arrow) and adventitial layer and smooth muscle layer of vessels (blue arrow) are marked.

The PAA-Gd agent exhibits high relaxivity because of its long main chain that results in a longer rotational correlation time at 7 Tesla. For DCE MRI, the sequence with short echo time (TE), repetition time (TR), and small flip angle (FA) (principally no more than $\pi/2$) was used to ensure scanning volumes with a high time resolution and high CNR. Because of the high relaxivity of PAA-Gd, the DCE sequence can provide high-contrast regions of interest (ROIs) *versus* other regions in biological tissues with a low dosage. Furthermore, the DCE acquisition would not require a long TR so that time resolutions could meet its utmost optimising parameter to match local longitudinal relaxation, which was reflected by eqn (3) in ESI.†

The cytotoxicity test demonstrated that the zwitterionic formed PAA-Gd had a low toxicity because of the negatively charged terminus inside the compounds, which resulted in a low probability of contact with the cell membrane. Thus, PAA-Gd exhibited enhanced biocompatibility and relaxivity.

3.2. Comparison of PAA-Gd *versus* low molecular weight compounds (LMWCs)

Numerous gadolinium-based agents that exhibit similar properties to PAA-Gd and LMWC, for example, Gd-DTPA, cannot be sieved by the vascular system and may extravasate to surrounding organs or tissues spontaneously.[28,29] Vascular permeability occurs constitutively for LMWCs, and similarly, the endothelium of tissues forms a semi-permeable barrier and allows transmembrane traffic of small components. The pathway leading to the kidney from the ISI site (Fig. 2b and 3b) is not observed on the DCE images of ISI with Gd-DTPA (ESI Fig. 5†). We propose that the difference can partially be derived from the relatively low relaxivity of Gd-DTPA compared to the PAA-Gd agent, so that the sites with low Gd^{3+} concentration are hard to observe with Gd-DTPA under the same MRI scanning parameters. Another possible explanation is that the relative molecular mass of Gd-DTPA is 938, which is much lower than the mass of PAA-Gd. The Gd-DTPA molecule *via* ISI may show a higher tendency of extravasation than directional movement along the interstitial stream. Therefore, the LMWC MRI agent may exhibit a high risk of leakage from fasciae and consequently cast blurring boundaries and high signal intensity in the whole body, namely a low CNR for interstitial stream imaging. However, PAA-Gd is confined inside fasciae along the interstitial stream because of its high molecular weight and can be used as a versatile agent for ISI imaging.

Although the relationship between tissues and fasciae has been reported,[30,31] the physiological readouts remain vague. The intricately woven LCT, namely fasciae, with fluid around tissues and organs hinders further anatomical study on healthy individuals because most clinically relevant studies are performed during surgery or clinical consultation.[32] Therefore, although the mechanical and thermal responses of the fascia system have received considerable attention, the anatomical structures and pathological alteration remain unclear; to investigate physiological behaviour, structural continuity and functional unity should be studied. The methodology to validate real-time imaging in the human body becomes necessary. MRI is an effective method for *in vivo* imaging and diagnosis of soft matter.

Theoretically, gadolinium-based macromolecular/nano-scaled agents are excellent candidates, not only for interstitial study. Recently, several T_1-enhanced nano-scale MRI contrast

agents have been reported.[33–35] The aforementioned features indicate that PAA-Gd exhibits considerable potential to trace the interstitial stream after ISI. The major merits of the PAA-Gd agent used for this study are as follows: (1) the property of its efficient magnetic contrasting effect with high relaxivity provides a high signal intensity and high contrast for MRI study. (2) The drastically shortened longitudinal time allows a low FA for the DCE sequence, and thus, it enables high time resolution in real-time acquisition. (3) The chromogenic reaction from purple to green reveals the distribution of PAA-Gd in biological tissues that can be viewed at the cellular level. (4) Mass spectrometry enables high precision analysis of trace gadolinium after distribution in the interstitium due to the absence of background Gd^{3+}. (5) The PAA-Gd agent completes the joint analysis from macro to micro, which provides comprehensive physiological readouts in the interstitial stream *in vivo*, *ex vivo*, and/or *in vitro*. Further estimation *via* histochemical study and analysis with mass spectrometry can be guided by the MRI results. Thus, the PAA agent with a diameter of 6 to 7 nm was confined in LCT without leakage into the blood vessel, which revealed that it can be used as a high-performance enhancer and specifically for interstitial stream research.

3.3. PAA-Gd application to reveal the route leading to the kidney

DCE imaging was performed for 20 min (Fig. 4a, ESI Movies 2 and 3†). The PAA-Gd delineated the renal hilus and cortex starting 5 min post-injection which lasted for more than 15 min, and the signal intensity strongly increased at the site of the hilus where the adventitia of the blood vessels merged into the tissue (Fig. 4c). This is further illustrated with a scheme in Fig. 4b.

The transportation of PAA-Gd in the interstitial stream is illustrated on the right side of Fig. 2a. The fabric bundles mainly comprised collagen microfibrils coupled with glycosaminoglycans on the intra-surface, which reduced the flow resistance.[7] Thus, the bundles facilitated the continuous transport of the macromolecular PAA-Gd agent along the path parallel to the vessels.

PAA-Gd with high relaxivity can be applied as a strong enhancer for intravital MRI study at the macro level, and its histochemical analysis was performed at the microscopic level through CPN III staining. The renal hilus and cortex contain LCT (Fig. 4d) and adipose tissue, which prevent the mass leakage of the macromolecule agent to the vascular system or other organs. The lightened path from the ankle to the kidney and the high signal intensity at the renal hilus and cortex supports the conjecture that the high-efficiency pathway starts from the tarsal tunnel at the ankle, traverses the para-vascular pathway, and leads to the kidney tissue through the interstitial stream constructed by fascia. The *in situ* images of DCE performed at 7 Tesla with a high SNR and resolution under optimised parameters, such as TE, TR, and FA, were obtained. The corresponding histochemical slice provided additional physiopathological information, which could be used to develop its application in *ex vivo* biopsy. The PAA-Gd agent can detect the interstitial stream with high specificity and sensitivity in the body.

The results reveal that PAA-Gd can reveal and trace the transportation and distribution post-injection along the ISI pathway, especially within the interstitial stream, and can be analysed with the histological analysis method of CPN III staining.

Gadolinium can react chromogenically with CPN III and thus distinguish the contrast dwell area from other tissues for effective combination of dynamic tracking and pathology in imaging.

3.4. Comparison of ISI and IVI using PAA-Gd

Trace quantification of elemental gadolinium by ICP-MS complements the information lacking in imaging and pathology for low concentration trace analysis, confirming the difference in the distribution of elemental gadolinium between the two different modalities of IVI and ISI.

The transportation pathways of PAA-Gd injected through ISI and IVI differed considerably. The first-pass effect is obvious in the IVI group, with the enhancement of the main vessels and the whole kidney clearly visible in the DCE images. The transportation of the PAA-Gd agent in the interstitial pathway differs according to its speed and routine, as the renal hilus and cortex have an enhanced signal in the ISI group. However, the blood flow motivates the spread of most MRI agents in the body, along arteries, veins, and blood capillaries in the IVI group.

The vessel membrane and tissue fascia form a barrier for macromolecules. Low leakage of the macromolecule agent PAA-Gd was determined with further ICP-MS tests and histochemical staining. For the ISI group, compared with the IVI group, there is a lower gadolinium content in the blood and an uneven content in tissues. The sample of the ipsilateral femoral vein of injection, where the signal enhancement is visible in DCE images, has a higher content of Gd^{3+} than other samples, including the blood sample. The non-blood portion of the vein provides a major contribution to the gadolinium content. Therefore, it can be determined that the Gd^{3+}-based PAA agent transports along the interstitial space paravascularly (ESI Movies 4 and 5†).

The histochemical result verifies the low leakage of the PAA-Gd agent from the interstitial stream. The MRI signal was mostly contributed by the agent transported *via* non-blood motivated transportation. The histochemical study shows the long duration of the PAA-Gd agent in the renal parenchyma for the ISI group, compared to the absence of the PAA-Gd agent after several minutes in the IVI group.

The results are of significant importance for robust imaging of the interstitial stream. This study has provided a typical manifestation of interstitial stream visualisation on the transportation of mass from the skin to the kidney using PAA-Gd, with high relaxivity and low leakage from the interstitium.

4. Conclusion

The PAA-Gd agent exhibits high relaxivity because of its long main chain that results in a longer rotational correlation time at 7 Tesla. Moreover, the agent with a diameter of 6–7 nm was

confined in LCT with low leakage into the blood vessel, which revealed that it can be used as a high-performance enhancer and can be used specifically in interstitial stream research. The *in situ* images of DCE performed at 7 Tesla with a high SNR and resolution under optimised parameters such as TE, TR, and FA was obtained. The corresponding histochemical slice provided additional physiopathological information, which could be used to develop its application in *ex vivo* biopsy.

The related phenomena indicate the long-range fluid behaviour of the interstitial stream, which may provide a novel method for the diagnosis and treatment of diseases. Clarifying the connection and path of various parts of the body under various physiological conditions of diseases provides a novel perspective for understanding the body and life activities.

Thus, by focusing on the structure–behaviour–function coupling mechanism of the interstitial structure and developing and perfecting the theory of interstitial stream, we can detail molecular biology and biochemistry, bridge the gap of the molecular mechanism to the macro-function, and enrich and develop the modern medical system.

Author contributions

X. Z. conducted most experiments and wrote the manuscript under the guidance of D. H., W. L. and Y. H. J. C. synthesised and characterised the agent and wrote the corresponding part of the manuscript under guidance from Y. H. and P. Z. X. Z. and F. H. conducted MRI experiments and processed images under guidance from W. L. and D. H. J. W. guided the experiments on the 1.5T MR scanner. W. T. assisted in the MR experiments on the 1.5T MR scanner. Q. L. assisted with animal anaesthesia and surgeries. X. Z., J. C. and P. Z. were responsible for the image design. Z. A. helped to analyse the data from ICP-MS and process the figures. X. Z. developed the code for calculation and imaging analysis, under guidance from W. L. Y. Z. helped to conduct the experiment of lymphangiography *versus* interstitial stream imaging using intravital microscopy *in vivo* and helped to edit the manuscript. Y. L. helped edit and polish the manuscript. All authors discussed the results and commented on the manuscript.

Conflicts of interest

There are no conflicts to declare.

Acknowledgements

This work was financial supported by the National Natural Science Foundation of China (No. 61971151) and financial support is highly appreciated.

References

1 J. Casley-Smith and A. Vincent, *Tissue and Cell*, 1978, **10**, 571–584.
2 I. Levental, P. C. Georges and P. A. Janmey, *Soft Matter*, 2007, **3**, 299–306.
3 J. Casley-Smith and A. Vincent, *Tissue and Cell*, 1980, **12**, 761–771.
4 L. Xie, H. Kang, Q. Xu, M. J. Chen, Y. Liao, M. Thiyagarajan, J. O'Donnell, D. J. Christensen, C. Nicholson and J. J. Iliff, *science*, 2013, **342**, 373–377.
5 J. J. Iliff, M. Wang, Y. Liao, B. A. Plogg, W. Peng, G. A. Gundersen, H. Benveniste, G. E. Vates, R. Deane and S. A. Goldman, *Sci. Transl. Med.*, 2012, **4**, 147ra111.
6 J. Feng, F. Wang, X. Han, Z. Ao, Q. Sun, W. Hua, P. Chen, T. Jing, H. Li and D. Han, *Nano Res.*, 2014, **7**, 434–442.
7 X. Han, H. Li, W. Hua, L. Dai, Z. Ao, F. Liao and D. Han, *Clin. Hemorheol. Microcirc.*, 2017, **67**, 173–182.
8 R. A. Jones, *Soft condensed matter*, Oxford University Press, 2002.
9 P.-G. De Gennes, *Science*, 1992, **256**, 495–497.
10 X. Shi, Y. Zhu, W. Hua, Y. Ji, Q. Ha, X. Han, Y. Liu, J. Gao, Q. Zhang and S. Liu, *Nano Res.*, 2016, **9**, 2097–2109.
11 N. Hu, Y. Cao, Z. Ao, X. Han, Q. Zhang, W. Liu, S. Liu, F. Liao and D. Han, *Nano Res.*, 2018, **11**, 2265–2276.
12 N. Hu, X. Shi, Q. Zhang, W. Liu, Y. Zhu, Y. Wang, Y. Hou, Y. Ji, Y. Cao and Q. Zeng, *Nano Res.*, 2019, **12**, 2760–2765.
13 P. C. Benias, R. G. Wells, B. Sackey-Aboagye, H. Klavan, J. Reidy, D. Buonocore, M. Miranda, S. Kornacki, M. Wayne and D. L. Carr-Locke, *Sci. Rep.*, 2018, **8**, 1–8.
14 H. Li, C. Yang, K. Lu, L. Zhang, J. Yang, F. Wang, D. Liu, D. Cui, M. Sun and J. Pang, *Clin. Hemorheol. Microcirc.*, 2016, **63**, 411–421.
15 H. Li, C. Yang, Y. Yin, F. Wang, M. Chen, L. Xu, N. Wang, D. Zhang, X. Wang and Y. Kong, *Cell Proliferation*, 2019, **52**, e12667.
16 T. Nakada, *Brain Dev.*, 2007, **29**, 325–335.
17 R. W. Brown, Y.-C. N. Cheng, E. M. Haacke, M. R. Thompson and R. Venkatesan, *Magnetic resonance imaging: physical principles and sequence design*, John Wiley & Sons, 2014.
18 A. H. Schmieder, S. D. Caruthers, J. Keupp, S. A. Wickline and G. M. Lanza, *Engineering*, 2015, **1**, 475–489.
19 H.-J. Weinmann, W. Ebert, B. Misselwitz and H. Schmitt-Willich, *Eur. J. Radiol.*, 2003, **46**, 33–44.
20 H. Y. Li, M. Chen, J. F. Yang, C. Q. Yang, L. Xu, F. Wang, J. B. Tong, Y. Lv and C. Suonan, *PLoS ONE*, 2012, **7**(7), e41395.
21 T. Chikui, M. Obara, A. W. Simonetti, M. Ohga, S. Koga, S. Kawano, Y. Matsuo, T. Kamintani, T. Shiraishi and E. Kitamoto, *Int. J. Dent.*, 2012, **2012**.
22 S. Jiang and Z. Cao, *Adv. Mater.*, 2010, **22**, 920–932.
23 I. M. Noebauer-Huhmann, P. Szomolanyi, V. Juras, O. Kraff, M. E. Ladd and S. Trattnig, *Invest. Radiol.*, 2010, **45**, 554–558.
24 J. Huang, Y. Hou, T. Ma, P. Zhang, Y. Li, C. Liu, B. Zhang, S. Qiu, J. Zeng and M. Gao, *Adv. Ther.*, 2018, **1**, 1800005.
25 D. Pan, A. H. Schmieder, S. A. Wickline and G. M. Lanza, *Tetrahedron*, 2011, **67**, 8431.
26 M. Spanoghe, D. Lanens, R. Dommisse, A. Van der Linden and F. Alderweireldt, *Magn. Reson. Imag.*, 1992, **10**, 913–917.
27 L. M. De León-Rodríguez, A. F. Martins, M. C. Pinho, N. M. Rofsky and A. D. Sherry, *J. Magn. Reson. Imag.*, 2015, **42**, 545–565.
28 L. Claesson-Welsh, *Upsala J. Med. Sci.*, 2015, **120**, 135–143.

29 G. Egawa, S. Nakamizo, Y. Natsuaki, Y. Miyachi and K. Kabashima, *Sci. Rep.*, 2013, **3**, 1–6.
30 W. Lowe and L. Chaitow, in *Orthopedic Massage*, ed. W. Lowe and L. Chaitow, Mosby, Edinburgh, 2nd edn, 2009, pp. 13–25, DOI: **10.1016/B978-0-443-06812-6.00002-7**.
31 C. Stecco, W. Hammer, A. Vleeming and R. De Caro, in *Functional Atlas of the Human Fascial System*, ed. C. Stecco, W. Hammer, A. Vleeming and R. De Caro, Churchill Livingstone, 2015, pp. 141–184, DOI: **10.1016/B978-0-7020-4430-4.00005-1**.
32 B. Bordoni and E. Zanier, *Journal of Multidisciplinary Healthcare*, 2014, 401–411.
33 Y. Yang, S. Chen, H. Li, Y. Yuan, Z. Zhang, J. Xie, D. W. Hwang, A. Zhang, M. Liu and X. Zhou, *Nano Lett.*, 2019, **19**, 441–448.
34 W. Yang, C. Xiang, Y. Xu, S. Chen, W. Zeng, K. Liu, X. Jin, X. Zhou and B. Zhang, *Biomaterials*, 2020, **255**, 120186.
35 Y. Li, X. Zhao, X. Liu, K. Cheng, X. Han, Y. Zhang, H. Min, G. Liu, J. Xu, J. Shi, H. Qin, H. Fan, L. Ren and G. Nie, *Adv. Mater.*, 2020, **32**, e1906799.